



2018 SAE Design Report
University of Tulsa
Regular Class

Team Members:

Kelly Shelts - Team Leader

Jarrold Braun

Garrett Carson

Duy Van

Fahad Ansari

Ryan Ogilvie

Hossam Dawood

Othman Al-Yousef

Glenn Lane



Faculty Advisor
Dr. Jim Sorem

Table of Contents	Page Number
Statement of Compliance	2
List of Figures and Tables	3
1.0 Executive Summary	3
2.0 Schedule Summary	4
3.0 Budget	5
4.0 Fluid Analysis and Airframe Design	5
4.1 Airfoil Analysis	5
4.2 Weight Capacity Analysis Techniques	6
4.3 Simulation	9
4.4 Final Wing Selection	11
4.5 Stability	12
5.0 Structural Design	14
5.1 Wing	14
5.2 Fuselage	15
5.3 Tail	16
5.4 Landing Gear	17
5.5 Connections	18
6.0 Manufacturing and Material Selection	19
7.0 Electronics	20
7.1 Motor and Propeller	20
7.2 Electrical System	22
8.0 Loading and Environmental Assumptions	22
9.0 Structural Analysis	23
9.1 Wing	23
9.2 Tail	24
9.3 Tube	24
9.4 Landing Gear	25
10.0 Servo Sizing	26
11.0 Conclusions	27
12.0 Table of Referenced Documents, References, and Specifications	27
List of Symbols and Acronyms	27
Appendix A: Payload Prediction Curve Density Altitude	28
Appendix B: 2D Drawing	29

SAE AERO DESIGN


STATEMENT OF COMPLIANCE

Certification of Qualification

Team Name University of Tulsa Regular Team Number 010
 School University of Tulsa
 Faculty Advisor Dr. James Sorem
 Faculty Advisor's Email james-sorem@utulsa.edu

Statement of Compliance

As Faculty Advisor, I certify that the registered team members are enrolled in collegiate courses. This team has designed, constructed and/or modified the radio controlled aircraft they will use for the SAE Aero Design 2018 competition, without direct assistance from professional engineers, R/C model experts or pilots, or related professionals.



Signature of Faculty Advisor

Team Captain Information:

Team Captain:	Kelly Shelts
Captain's E-mail:	kelly-shelts@utulsa.edu
Captain's Phone:	918-914-3127

Note:

A copy of this statement needs to be included in your Design Report as page 2 (Reference Section 4.3)

List of Figures and Tables

Tables		Figures	
1.0.1	Competition Design Requirements	2.0.1	Fall 2017 Schedule
1.0.2	Projected Performance	2.0.2	Spring 2018 Schedule
3.0.1	Material Cost	4.2.1	Generic Graph of Drag Coefficient Versus Velocity
4.1.1	Airfoil Analysis	4.3.1	Allowable Weight for Different Variables
4.4.2	Scoring Equation	4.3.2	Net Weight for Different Variables
4.5.1	Horizontal Stabilizer Dimensions	4.4.1	Final Wing Design
4.5.2	Vertical Stabilizer Dimension	4.5.1	Longitudinal Root Locus Plot
5.1.1	Wing Dimensions	4.5.2	Lateral Stability Root Locus Plot
5.2.1	Key Fuselage Dimensions	5.1.1	Wing Rendering
5.3.1	Wing and Tail Dimensions	5.1.2	Wing Cross Section View
6.0.1	Wood Comparison	5.2.1	Fuselage Rendering
7.2.1	Electronics	5.2.2	Slider Weight Box
8.0.1	Critical Loads and Sources	5.3.1	Tail Section Vertical and Horizontal Stabilizer
9.1.1	Spar Shape Comparison	5.4.1	Landing Gear
9.3.1	Tube Stresses	5.4.2	Landing Gear Placement
9.4.1	Landing Gear Stresses	5.5.1	Exploded View
10.0.1	Necessary Servo Torques for Control Surface	6.0.1	Cut-out Parts
		7.1.1	Graph of Force for Velocity Given a Propeller with a 260 KV Motor
		7.1.2	Prop Diameter Versus Force Test Results
		7.1.3	Test Stand Setup
		9.1.1	Proposed Spar Configuration
		9.3.1	Tube Load Application

1.0 Executive Summary

The SAE Aero Design Challenge is an international collegiate competition in which students compete to design, manufacture, test, and fly remote controlled airplanes to score points. The regular class competition simulates real life challenges by requiring the aircraft to carry both passengers and cargo, modeled with tennis balls and weights. The goal of the competition is to carry the largest amount of passengers and cargo given several design constraints. The competition design requirements are shown below in Table 1.0.1.

Table 1.0.1 Competition Design Requirements

Wattage	<1000 Watts	Flight Circuit	1 Loop
Wingspan	<12 ft	Max Plane and Cargo Weight	55 Pounds
Battery	22.2V Lithium Polymer, Min 3000 mah	Motor	Electric
Takeoff	< 200 ft	Materials	No Fiber reinforced plastics

The 2018 TU plane utilizes a single 12 foot long backward swept wing, a 10 foot long fuselage, and a tail section consisting of horizontal and vertical stabilizers. The plane was designed to be as light as possible, while still being able to carry as much weight as possible. Iterative design and analysis was performed to maximize performance, the results of which are shown in Table 1.0.2. The strategy for this season was to build a reliable plane with exchangeable parts so that it can complete each round. This is done by optimizing airframe design to maximize lift, minimize drag, and reduce the weight of the plane so as to maximize the number of passengers and cargo loads that may be carried. Test flights of this year's plane were also successfully performed prior to design submission in order to verify the predictions shown in Table 1.0.2

Table 1.0.2 Projected Performance

Plane Weight	17.3 lbs
Wing area	19.2 ft ²
Max weight	31.7 lbs
Carried weight	13.8 lbs
Score	68.7

The TU SAE Aero team is unique in that TU does not have an aerospace engineering program and all students on the team study mechanical engineering. This provides an additional challenge that has motivated the team to do extra research and testing to learn about aerodynamic and airplane structural principles in order to be as competitive as possible.

2.0 Schedule Summary

In order to complete this task, design work started in Fall 2017, shown below in Figure 2.0.1.

	September 25-October 1	October 2- 8	October 9-15	October 16-22	October 23-29	October 30-November 5	November 6 - 12	November 13-19	November 20-26	November 27-Dec 3
Test Fly 2017 Plane										
Air Frame Design (CFD)										
Structural Design Brainstorming										
Research Vendors										
Propeller and Motor Test										
Solidworks										

Figure 2.0.1: Fall 2017 Schedule

A spring semester schedule is shown below in Figure 2.0.2.

	Jan 8-14	Jan 15-21	Jan 22-28	Jan 29-Feb 4	Feb 5-11	Feb 12-18	Feb 19-25	Feb 26-Mar 4	Mar 5-11	Mar 12-18	Mar 19-25	Mar 26-Apr 1
Finish Structural Design												
Structural Analysis												
Order Parts												
Build Frame												
Cover Frame												
Install Electronics												
Test Flight												
Repairs, Improvements												
Write Report												
Create Presentation												
Practice Presentation												
Build Spare Parts												

Figure 2.0.2 Spring 2018 Schedule

3.0 Budget

The material cost is listed in Table 3.0.1. In comparison with past TU planes, this plane was significantly more expensive. This is due to the use of higher quality materials and components, which improved the plane. For example, a lower quality sheeting was used in past years, causing wrinkles, tears, and dimpling, which caused excessive drag at the frontal surface of the wings. This year, higher quality MonoKote and specialized application tools were purchased, reducing problems that arose with the cheaper alternative.

Table 3.0.1: Material Cost

Materials	
Items	Costs (\$)
Motor & ESC	130.37
Battery & charger	185.52
Receiver	39.99
Servos	127.14
Other Electronic components	168.73
Total	651.75
Balsa	342.37
Spruce	569.88
Aluminum	353.31
Airplane related components	268.88
Total	1534.44
Monokote	358.87
Glues & Epoxy	64.9
Other tools	482.52
Total	906.29
Materials total cost	\$ 3,092.48

4.0 Fluid Analysis and Airframe Design

4.1 Airfoil Analysis

Wing design begins with choosing an airfoil, the shape of the wing's profile, which determines the wing's lift and drag coefficients (C_L and C_D). The team analyzed five high lift airfoils: the NACA 9312, FX74 CL5, CH10, S1210, and S1223. The foils were analyzed using Computational Fluid

Dynamics (CFD) and software XFLR5 using a base chord length of 1 ft . The analysis was run using a constant Reynold's Number of 295,276, calculated using the density of air at sea level and a velocity of approximately 27 mph. and varying angles of attack. Chart 4.1.1 summarizes the findings for comparison.

Table 4.1.1: Airfoil Analysis

Airfoil	C_L at 0°	C_D at 0°	C_L/C_D at 0°	Max C_L
NACA 9312	0.844	0.019	44.6	1.5
FX74 CL5	1.09	0.025	41.8	1.62
CH10	0.93	0.024	39.5	1.62
S1210	0.99	0.018	55.7	1.77
S1223	1.11	0.02	55.3	1.84

The Selig 1223 airfoil was chosen for the main wing because it has the highest C_L at an angle of zero degrees, 1.11 It also has the highest maximum C_L of 1.84. Additionally, this foil has a high ratio of C_L/C_D and a low C_D at an angle of attack of zero degrees. However, the S1210 has extremely similar properties. To determine which would actually perform better, two identical wing shapes were simulated using the techniques discussed in Section 4.2, one with the S1223 airfoil and one with the S1210 airfoil. The S1223 wing had a higher weight-capacity than the S1210 wing, so the S1223 airfoil was chosen for all further wing simulations and for the final wing design.

4.2 Weight Capacity Analysis Techniques

The team developed a thorough method for determining the weight capacity of the airplane for for both take-off and in-flight conditions. This is crucial for performing well at the competition, since the flight score is dependent on the passenger and luggage capacity of the aircraft. The approach begins with a C_D versus velocity data for a wing with the S1223 airfoil profile, obtained via Computational Fluid Dynamics, show below in Figure 4.2.1.

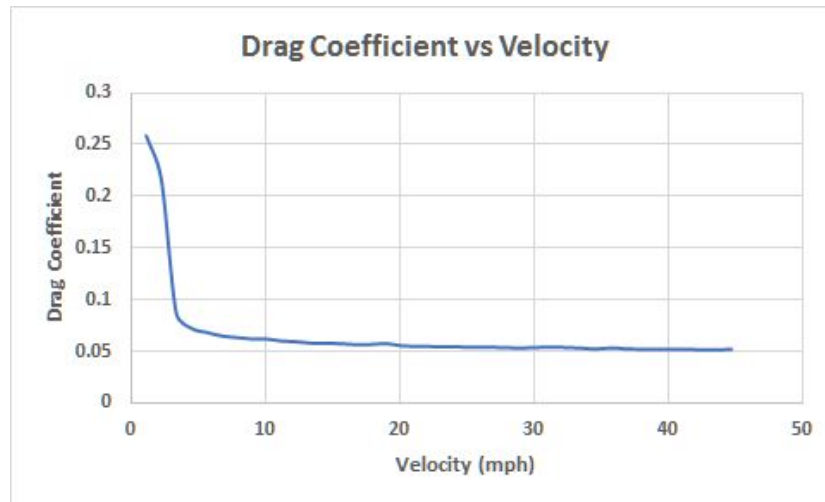


Figure 4.2.1: Generic Graph of Drag Coefficient Versus Velocity

The team wrote a program that creates a piecewise continuous function based on the drag coefficient data obtained from XFLR5. This function changes for each plane tested because each plane has different drag characteristics. Since the drag force is dependent on the drag coefficient, the following equation can be used to calculate net thrust:

$$T_{net}(v) = T(v) - D(v) - f(v)$$

Friction is a function of velocity because as the plane gains speed, lift increases, which reduces the normal force on the wheels from the ground. Acceleration at a specific velocity could then be calculated by dividing the net thrust by the mass of the aircraft. From the kinematic equations of constant acceleration.

$$X = x + vt + 0.5at^2 \quad \text{and} \quad V(v) = v + at$$

the distance the plane travels in a very small time increment and its velocity after that time period can be calculated, since acceleration may be considered constant during small time periods. By iterating and summing the distances traveled until takeoff velocity is reached, the total distance the plane travels during takeoff can be calculated. The value for takeoff distance was found to converge to two decimal places when the time increment reached 0.01 seconds.

In order to determine the maximum weight capacity of a wing, the takeoff distance calculator was programmatically repeated with increasing mass values until a takeoff distance of 200 feet was

reached. This calculation illustrates the linear relationship between takeoff distance and wing load capabilities.

However, takeoff weight capability is not the same as in flight cargo sustainability. The rotation of the plane on lift-off causes an increase in both lift and drag, which is taken into consideration in the takeoff analysis. However, the plane returns to a low angle of attack during cruising flight, lowering the lift coefficient and requiring a higher speed to maintain sufficient lift. To determine whether a plane is able to achieve the necessary speed, the velocity when the propeller thrust and drag force are equal was calculated. This becomes the maximum speed of the airplane. That velocity is then substituted into the following lift equation to find the maximum weight capacity in-flight, where the lift coefficient is at zero angle of attack:

$$L = \frac{1}{2} \rho v^2 A C_L$$

The lowest value of the takeoff and in-flight weight capacities is taken to be the limiting weight capacity of that wing. These calculations were performed neglecting the added lift from ground effect. This produces more conservative results.

Air properties were assumed to be those at sea level. However, as altitude increases the density of air varies, yielding different weight capacities at different heights. In accordance with the Technical Design Report and Technical Data Sheet requirements, the team captured the payload weight capacity vs altitude for the final design selected. To obtain this information the team calculated pressures and temperatures at various altitudes according to the following two equations:

$$p = p_0 \left(1 - \frac{Lh}{T_0} \right)^{\frac{gM}{RL}} \quad \text{and} \quad T = T_0 - Lh$$

where p_0 is the pressure at sea level, L is the temperature lapse rate, h is the altitude, g is acceleration due to gravity, M is the molar mass of air, R is the universal ideal gas constant, and T_0 is the temperature

at sea level. Air densities at altitudes ranging from sea level (0 ft) to 4000 ft were then calculated according to the ideal gas law:

$$\rho = \frac{pM}{RT}$$

The limiting weight capacities of the final wing design at those heights were determined based on the corresponding air densities. The results are shown in the appendix.

4.3 Simulations

More than 300 wing designs were simulated to calculate the maximum allowable weight generated using the methods described in Section 4.2. Four different independent variables of the wing design were considered to obtain the allowable weight: wingspan, root chord length, tip chord length, and taper start location. In order to give a visual of the data, the test points were gathered and presented in different 3D graphs.

Figure 4.3.1 illustrates the wing design with variable root chord length and wingspan as no taper is needed. The root chord is on the horizontal axis, ranges from 12 in to 30 in with 3 in increment and the wingspan is on the depth axis, ranges from 9 to 15 feet with 1 foot increment. The non-taper graph clearly shows that as the wingspan increases from 9 to 15 feet, the maximum allowable weight of the wing also increases. Because of this pattern and the wingspan limitation, the 12 feet wingspan was chosen not only as a fixed variable for the next analysis but also for the final wingspan selection.

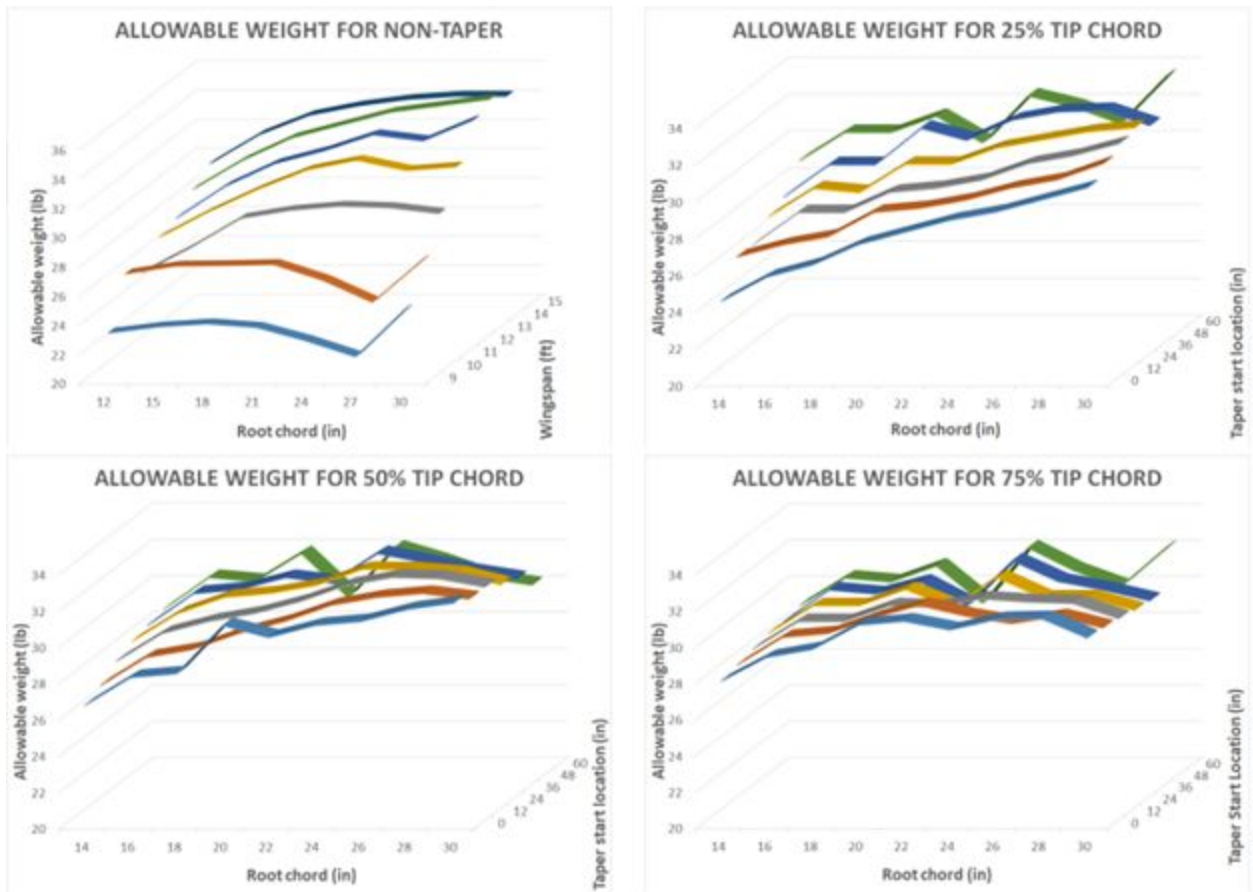


Figure 4.3.1: Allowable Weight for Different Variables

With a constant 12 foot wingspan, there were three independent variables left: tip chord length, root chord, and taper start location. The tip chord lengths considered were 25%, 50%, and 75% of the length of the root chord. A 3D graph was made for each tip chord length ratio, varying root chord length and taper start location to show the allowable weight of each wing. The three graphs are shown in Figure 4.3.1., which has the same root chord length variable on the horizontal axis, and the taper start location is on the depth axis. The three graphs similarly show that smaller wings with less surface area (smaller root chord length and short taper start location) generate less payload weight. This pattern is more noticeable with smaller tip chord percentage. However, this data cannot solely be used to determine the optimum wing design because as the wings get bigger, they do generate more lift but their own weight also increases as well. Their lifting weight has to compensate for their own weight. As a result, using the four graphs in Figure 4.3.1, net weight graphs were made by subtracting each wing design's allowable weight by their estimated wing weight. The graphs are shown in Fig 4.3.2 below.

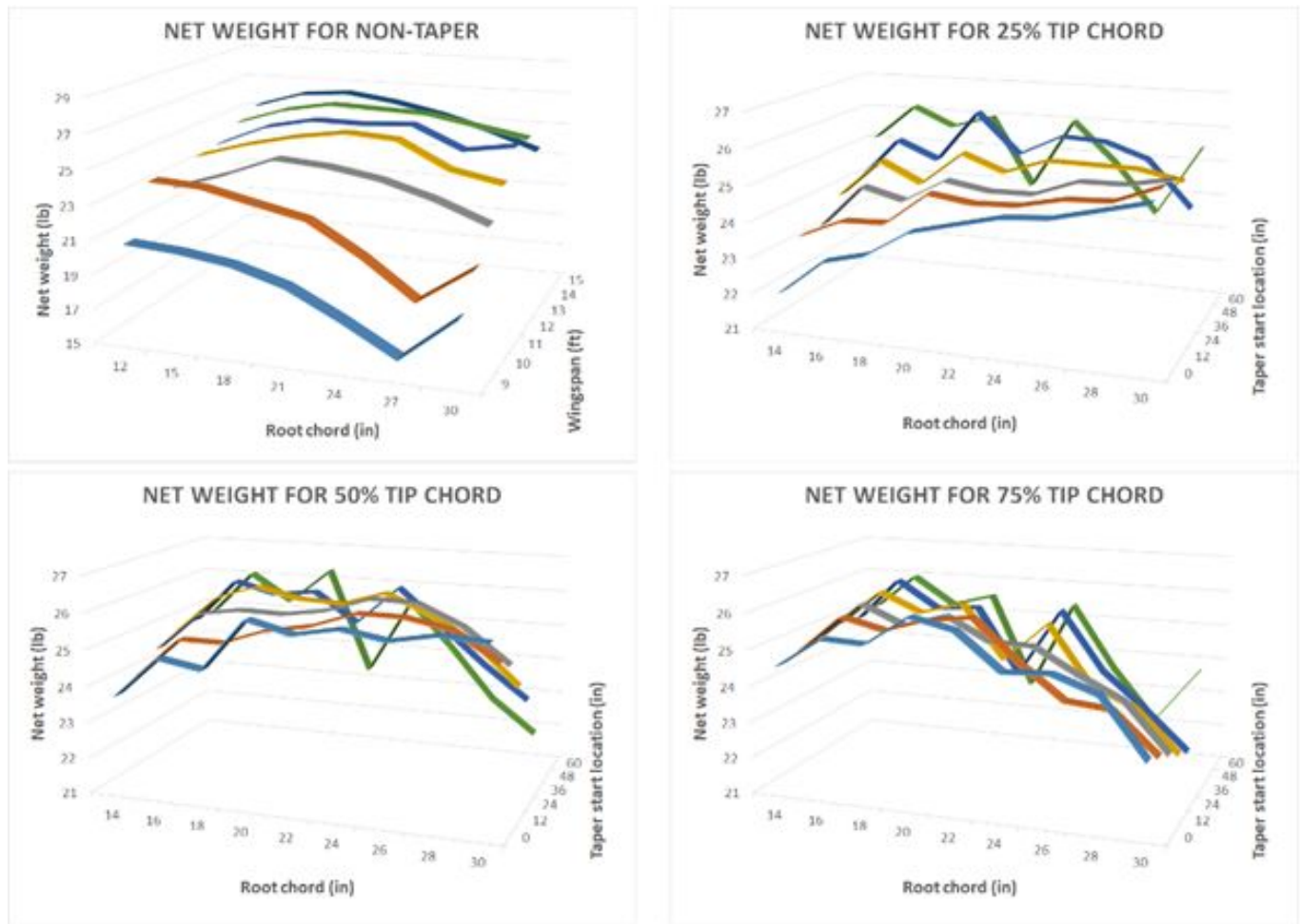


Figure 4.3.2: Net Weight for Different Variables

The four graphs all show a same pattern comparing the the allowable weight graphs: the net weight increases in the beginning and drops at the end as the wing reaches the 30 in root chord. This indicates that the wings with large root chord length have their weight increased more than the generated lift can compensate. As a result, the high net weight wings tend to have their root chord length between 18 and 24 in. This is one of the main factors used to determine the best wing design.

4.4 Final Wing Selection

Using the methodology presented in Sections 4.2 and 4.3, the wing shape shown in Figure 4.4.1 was selected for the final design. The wingspan is 12 feet with a 20 inch root chord and a 1 foot tapered section at the wingtips. The chord length at the wingtips is 10 inches. This wing was calculated to provide the highest net weight capacity. The simulated wing is able to lift 31.7 lbs at a takeoff distance

of 200 feet. The fully constructed airplane was weighed to be 17.3 lbs, leaving 14.4 lbs for passengers and luggage.

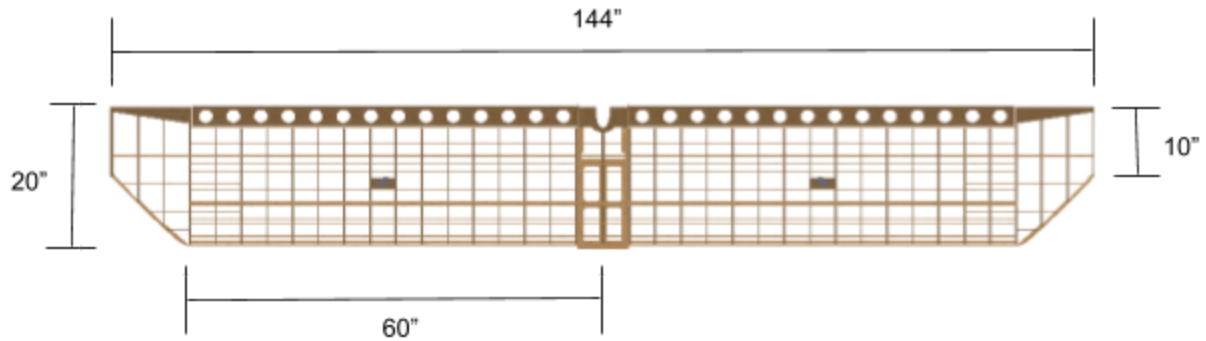


Figure 4.4.1: Final Wing Design

According to the per-round flight score equation (FS) in Figure 4.4.2, \$100 is awarded per passenger and only \$50 per pound of luggage. The score is maximized each round by carrying the most passengers since they are worth more per-unit than luggage. Therefore, the team calculated passengers carried using the minimum 0.5 lbs of luggage per passenger to allow for as many passengers as possible. Under these conditions the plane will be able to carry 22 passengers. This results in a per-round flight score of 2750 and a Final Flight Score of 68.75.

$$FFS = \text{Final Flight Score} = \frac{1}{40N} \left[\sum_1^N FS \right]$$

$$FS = \text{Flight Score} = \$100P + \$50C - \$100E$$

Figure 4.4.2: Scoring Equation

A test flight of the fully constructed plane verified the passenger and luggage calculations. The flight also revealed that the fully loaded airplane can take off in approximately 150 feet, significantly less than the 200 feet competition limit. The difference between the calculated and actual takeoff distances is likely due to conservative values for factors such as wheel deflection, which contributes to drag during takeoff.

4.5 Stability

Longitudinal stability is dependent on the horizontal stabilizer. The effectiveness of the stabilizer is represented in the root locus graph obtained from CFD software, shown in Figure 4.5.1. Each point on

the graph represents a longitudinal mode of oscillation. Points to the left of the imaginary axis reflect damped oscillations and points to the right reflect underdamped oscillations. All of the points on the longitudinal root locus graph for this plane indicate damped oscillations and stable flight. The real axis corresponds to a frequency of zero, and points further away from this axis have higher oscillatory frequencies. The overall behavior of the plane is a combination of the four modes.

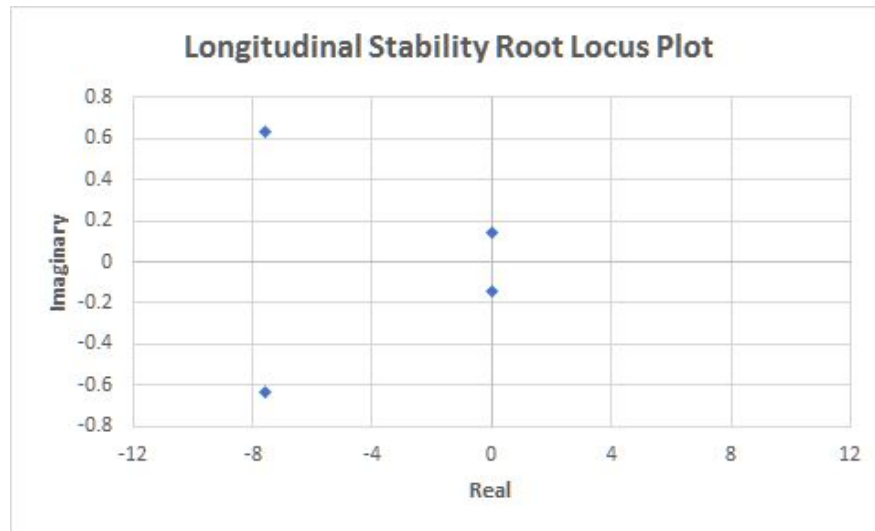


Figure 4.5.1: Longitudinal Root Locus Plot

The size and location of the horizontal stabilizer was adjusted iteratively to achieve damped oscillations with small frequencies while stabilizing the aircraft at zero angle of attack, where the wing achieves the highest lift to drag ratio. The horizontal stabilizer is placed 6 feet back from the leading edge of the wing. Specific dimensions are listed in Table 4.5.1 below as well as in the engineering drawing of the final design in the appendix.

Table 4.5.1: Horizontal Stabilizer Dimensions

	Span (in)	Chord Length (in)	Area (ft ²)
Horizontal Stabilizer	69	12	5.75

Lateral stability was also measured according to a root locus graph, shown in Figure 4.5.2 below. Stability was achieved using a center of gravity positioned below the wing and a vertical stabilizer placed 6 feet back from the leading edge of the main wing.

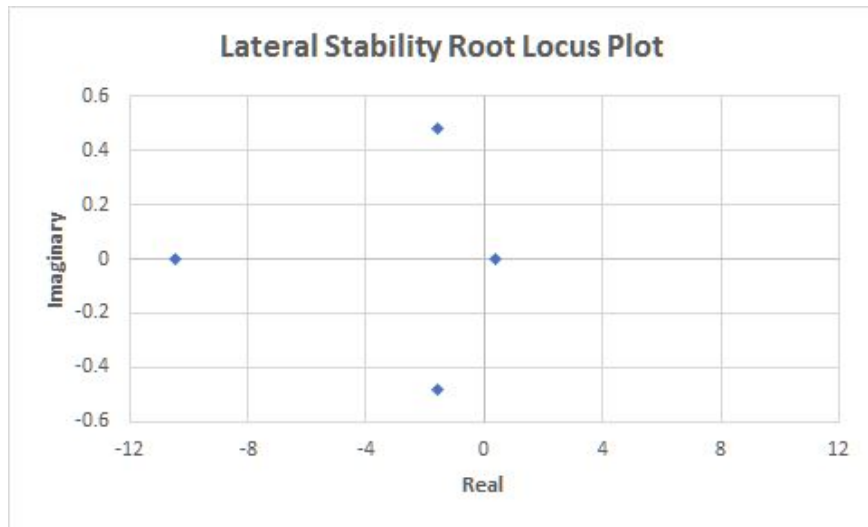


Figure 4.5.2: Lateral Stability Root Locus Plot

There is still one point to the right of the imaginary axis in the root locus graph, indicating one mode of instability. This is characterized by a tendency to very slowly continue in the direction of a yaw/horizontal disturbance. The team found that the only way to correct this was to incorporate a large amount of dihedral on the main wing but that would complicate manufacturing. Since a small yaw correction by the pilot would be sufficient to return the plane to normal flight, the team deemed the vertical stabilizer, low CG, and piloting ability sufficient for lateral stability. The dimensions for the vertical stabilizer are detailed in Table 4.5.2

Table 4.5.2: Vertical Stabilizer Dimensions

	Height (in)	Chord Length (in)	Area (ft²)
Vertical Stabilizer	24.25	12.4	2.088

5.0 Structural Design

5.1 Wing

The wing in Figure 5.1.1 was designed with balsa and spruce. The winglets reduce drag and turbulence at the wing tips by preventing air from slipping off the tip of the wings and forming vortices. Two major spars support the weight while smaller stringers help to support monokote attachment and add additional rigidity.

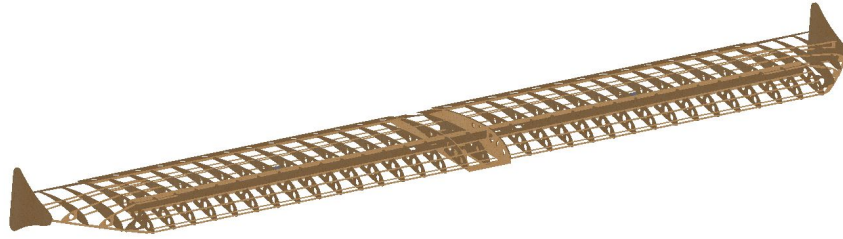


Figure 5.1.1: Wing Rendering

Table 5.1.1 lists all the major dimensions for the wing. The total area is roughly 20 ft² which gives us a high amount of area for lift. Lastly, the aileron was sized to be about 12% total area of the wing for both sides. This is a common percentage when designing planes.

Table 5.1.1: Wing Dimensions

Length	143.5 inches	Aileron Chord	4 inches
Chord	20 inches	Aileron Area	2.33 ft ²
Area	19.93 ft ²	Percent Area Aileron	11.7%
Aileron Length (half)	56 inches		

Figure 5.1.2 shows a cross section of the wing to illustrate the final form of the S1223 airfoil. The main support spars are placed on the wing 6 inches back from the leading edge which is about where the center of lift of the plane is. An I-Beam configuration is made by adding a small balsa section to act as a web between the support spars. Lightening holes are used to reduce weight.

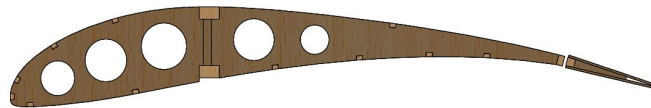


Figure 5.1.2: Wing Cross Section View

5.2 Fuselage

The fuselage and landing gear are shown in Figure 5.2.1. The battery and ballast box are placed 1.75 inches behind the propeller motor to ensure ideal center of gravity (CG) location. The propeller and motor are held by ¼” thick spruce.

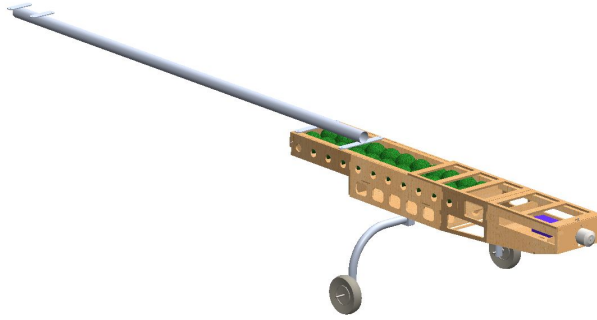


Figure 5.2.1: Fuselage Rendering

Table 5.2.1: Key Fuselage Dimensions

Length (motor plate to tail trailing edge)	9.26 ft
Wheel separation	24"
Angle at rest	8.5 degrees

The weights have a hole in the center and fit onto a threaded rod. Their location can be moved fore and aft with wing nuts to adjust the plane's CG. The CG is between 5" and 6.5" from the leading edge. The weight box slides into the back of the fuselage box and is held in place with a bolt.

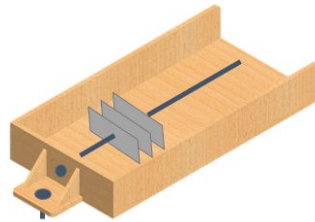


Figure 5.2.2: Slider Weight Box

The wing and tail section are connected with a 1.5" OD, 0.035" wall thickness aluminum tube. The tube has plates welded to create the attachment points for the fuselage box and tail section.

5.3 Tail

The tail assembly found in Figure 5.3.1 is comprised of spruce spars with balsa profiles.

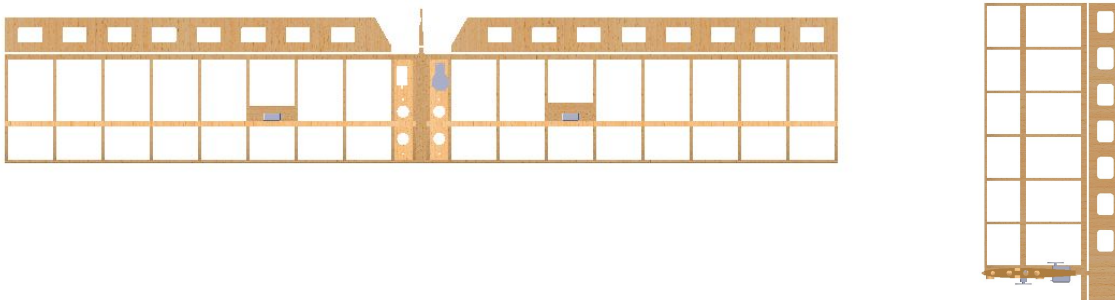


Fig 5.3.1 Tail Section Vertical and Horizontal Stabilizer

The elevator is split to accommodate the rudder. The base mounting plate is ½” spruce to connect to the fuselage. Servo mounts are placed between ribs. Rib spacing was chosen to be 4” to minimize monokote dimpling and contribute to the overall rigidity of the structure. Tail section profile for vertical and horizontal stabilizers was chosen to be NACA 0008 due to its symmetric airfoil and minimal drag characteristics during flight. The vertical stabilizer spars fit into slots on the horizontal stabilizer. To further increase rigidity between the horizontal and vertical stabilizers, bracing wires are installed.

The elevator was divided allow for the extension of the rudder below the horizontal by 3.25”. The tailwheel is then controlled by the rudder action through a spring a pivot system. Other possibilities for tailwheel control involved inserting a control rod into the rudder itself. The spring and pivot tailwheel control system was chosen to reduce the amount of hard attachment to the rudder in case of tailwheel support failure. In the case of failure, the aircraft rudder will still be operational.

Table 5.3.1: Wing and Tail Dimensions

Horizontal Length	69 inches	Vertical & Rudder Area	2.11 ft ²
Horizontal & Elevator Chord	12 inches	Vertical & Rudder Chord	12.4”
Elevator Length (Half)	32 inches	Rudder Area	0.76 ft ²
Elevator Chord	4 inches	Vertical length	24.25”
Percent Area Elevator	30.7 %	Rudder length	27.5”
Horizontal and Elevator Area	5.75 ft ²	Rudder Chord	4”
Elevator Area	1.77 ft ²	Percent Area Rudder	36.0%

A standard rule of thumb for control surface sizing was applied by using an approximate 25% of stabilizer to control surface area; the elevator was found to be 0.89 ft² while the rudder required 0.76ft². Control surfaces are mounted using heavy duty cotter pin hinges mounted within the trailing edge of the stabilizer and leading edge of the control surface. Using cotter pin hinges contribute to the rigidity of the control surface while reducing the amount of energy need to turn the hinge itself.

5.4 Landing Gear

The main landing gear was made from bent aluminum tubing with an outer diameter of 1.5” and wall thickness of .035” . The tail wheel was purchased, and is made steerable by attachment to the

rudder. The landing gear type is conventional, with a tail wheel that lifts off the ground once the plane reaches a certain velocity. The distance between the wheels is 24 inches for stability. Figure 5.4.2 shows the acceptable angles for a taildragger (8). These angles were placed in solidworks with given dimensions from the plane to determine wheel placement. The landing gear lifts the bottom of the fuselage 1 ft from the ground. The landing gear is placed 6 inches in front of the CG as an optimal distance for balance during takeoff (8). The wheels are high density foam with a rubber skin. In previous planes, foam wheels were used, which had large deflection and added significant drag. These wheels are rated for 50 lb planes for minimal drag.

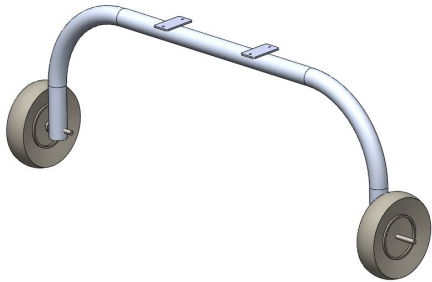


Figure 5.4.1: Landing Gear

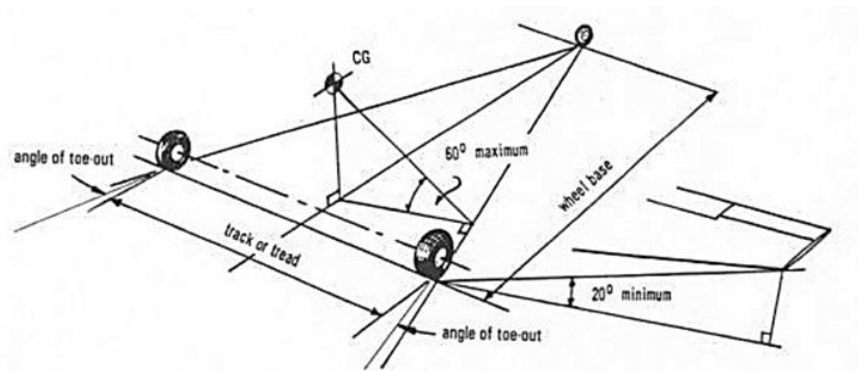


Figure 5.4.2 Landing Gear Placement (8)

5.5 Connections

The connections between the tail section, wing, landing gear, and fuselage are shown in Fig 5.6.1. The main connecting structure is the aluminum tube with welded plates. The tube mounts on top of the fuselage with, and the wing mounts over the tube onto the fuselage, both with bolted connections. The tail section bolts onto a welded plate on top of the tube. The landing gear bolts to the bottom of the fuselage, underneath the weight compartment. The tail wheel mounts to the bottom of the tube. All of the bolts connecting to the aluminum tube are #6-32.

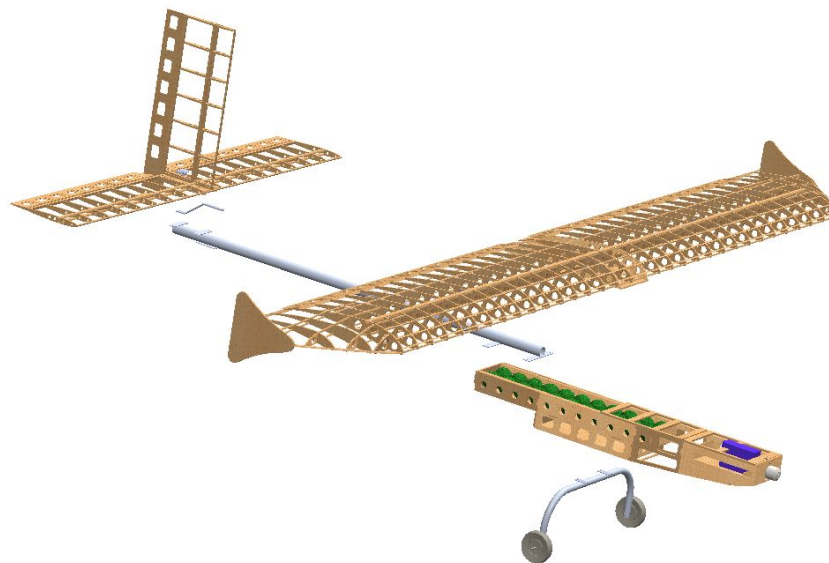


Figure 5.5.1: Exploded view

6.0 Manufacturing and Material Selection

The wing, tail and fuselage were all modified for ease of repairing parts. The wing and tail foils are made of balsa since the spruce spars hold the bending loads of the wing. These sections are laser cut for accuracy and then sanded and edge cleaned with alcohol before covering. CA adhesive was used to tack the parts together, then epoxy glue was applied to strengthen the connection. Notches are used for alignment. The tail section is made in two parts : horizontal, and vertical stabilizers made of balsa foils with spruce spars for the bending load during flight.

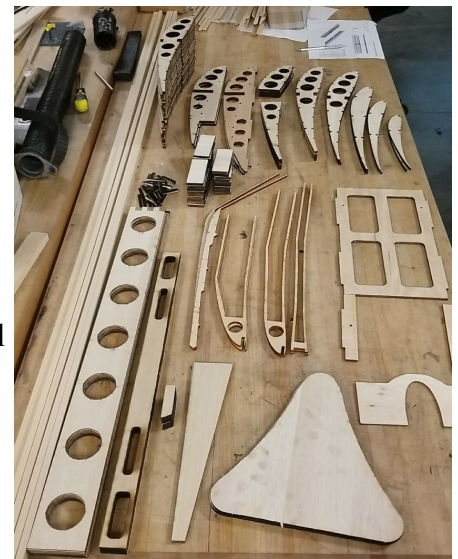


Figure 6.0.1: Cut-out Parts

The fuselage uses two main spruce beams to hold the loads of carrying the weight of both passengers and luggage. Those two beams lead into an aluminum tube since the length of the plane requires a higher yield strength from the torsional and bending during flight with possibly rough conditions. This could have been accomplished with thicker spruce beams or denser wood, but the ratio of strength to weight would be too high.

Balsa was chosen for the non-structural components because of its extremely low density and

sufficient strength. Spruce was chosen for its high strength to weight ratio and availability in specialized dimensions.

Table 6.0.1: Wood Comparison

Type of wood	Balsa	Spruce	Pine
Max shear strength (psi)	1000	1,230	1170
Density (lb/ft ³)	10	28	22
Strength to Weight Ratio (Shear strength/Density)	100	43.9	53.2

7.0 Electronics

7.1 Motor and Propeller

This year, analysis was done with a lower KV motor and a higher diameter prop because, according to advice that it is more efficient. The motor selected was a 260KV motor. Specifically, a Turnigy SK3-6354 260KV motor was chosen. Figure 7.1.1 explains how this propeller was chosen given this motor choice. Figure 7.1.1 shows how the effective thrust changes with velocity using a dynamic equation for thrust. The highest watt pull is expected at static thrust. Each line represents a different propeller diameter with a calculated pitch that would give 1000 Watts for static thrust.

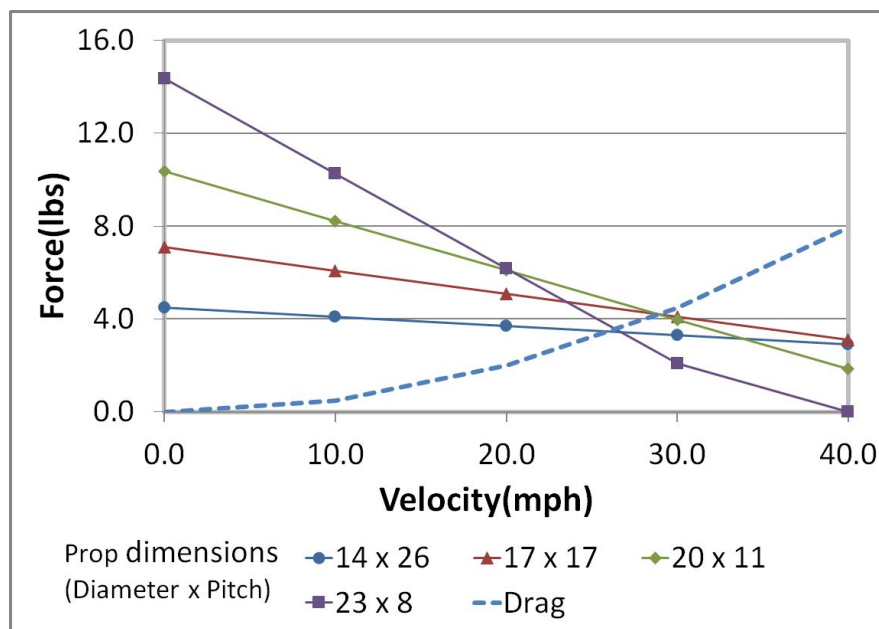


Figure 7.1.1: Graph of Force for Velocity Given a Propeller with a 260KV Motor

The analysis in Figure 7.1.1 illustrates the performance of various motor and propeller combinations. A high diameter - low pitch propeller such as the 23 x 8 would give high initial thrust

during takeoff but has lower thrust during flight. Alternatively, a high pitch - low diameter propeller would give low thrust at takeoff but higher thrust at high velocities. The maximum velocity can be determined by the intersection of the drag curve and the thrust curve. The intersection with the highest velocity is the propeller chosen to further analyze. For Figure 7.1.1 it appears the 17" x 17" prop and the 20" x 11" prop are the best and have about the same intersection. However, since they are the same, the 20" x 11" has a higher initial thrust which can improve takeoff. Therefore the 20" x 11" was picked as a start for a propeller to test with for a 260KV motor.

The next step would be to order the most equivalent props available to the 20" x 11" propeller and run static prop tests. Different types and different manufacturers were selected to test props this year including Graupner or APC propellers and wide or electric propellers. The manufacturer type did not seem to have much effect on results and predictions. However, wide style propellers varied significantly from electric propellers. The wide propellers are much thicker and heavier and based on predictions it gave a 32% error. All electric propellers were within 12% error. Last years propellers were also compared. Figure 7.1.2 and 7.1.3 show how the static tests were run and the results. In Figure 7.1.3 a right angle wood assembly is hinged so the force of the propeller can act and be read by the scale. Figure 7.1.3 pictures the motor tests done with both low KV - high diameter propellers and lower diameter propeller - higher KV motors.

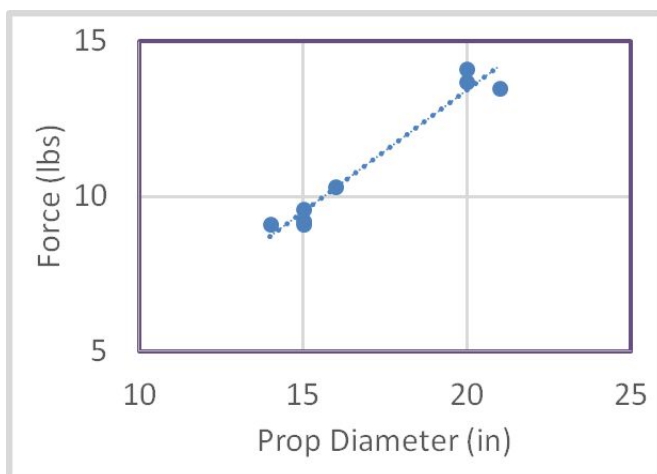


Figure 7.1.2: Prop Diameter Versus Force Test Results



Figure 7.1.3: Test Stand Setup

Figure 7.1.2 helps to illustrate the improved effect larger propeller lower KV motor systems have. For static thrust there is a 40% increase in thrust. This helps us to verify the assumption at the beginning of this section that these systems are more efficient. Therefore, a larger prop with a lower KV motor was placed on our plane this year. Specifically, a Graupner 20" x 10" E propeller was chosen. While the APC wide propeller gave slightly better results, the Graupner electric propeller was chosen over the APC prop because it was both lighter and had less vibrations.

7.2: Electrical Systems

Once the propeller and motor are chosen the rest of the components are chosen. These components are all listed in Table 7.1.1 The battery at 3300mAh was determined to have a flight time of about 10 minutes which is plenty for one round of flight. The maximum current at 22V for 1000 watts is expected around 45 Amps. Therefore the Talon 90 Amp ESC and the XT60 connectors which can handle up to 60 amps are both rated appropriately for these requirements. Since a long length of wire is required for the arming plug, thicker 10 awg wire was chosen to help reduce power loss.

Table 7.2.1 Electronics

ESC	Talon 90A ESC
Battery	Turnigy Nano-tech 3300mAh, 6S, 25-50C
Wire	10 awg
Connectors	XT60
Propeller	Graupner 20x10E
Motor	Turnigy SK3-6354 260KV

8.0 Loading and Environmental Assumptions

The loading applied in Sections 9 and 10 comes from three main sources: lift from the wing, weight of the stabilizers, and forces generated by deflecting the tail control surfaces. Control surface loads were calculated by modeling the surfaces as flat plates that receive the dynamic pressure created by the air's relative velocity as the plane flies. The surfaces were assumed to be fully deflected at 40 degrees to capture the maximum force acting on each surface, perpendicular to and at the center of each surface.

Impact force on the landing gear was calculated by determining vertical acceleration during landing and multiplying by the mass of the airplane. Conservative values for a descent rate on landing and impact time were 4.5 mph and 0.1 seconds respectively. These were used to compute impact acceleration, and finally an impact force. Table 8.0.1 details all forces considered in Section 9 and 10 and their sources.

Table 8.0.1: Critical Loads and Sources

Source	Force (lbs)
Wing Lift	31.70
Elevator	2.86
Rudder	1.19
Aileron	1.82
Tail Section Weight	1.3
Landing Impact	100

9.0 Structural Analysis:

9.1 Wing

When analyzing wing strength, bending was considered the most critical load, so the equation bending stress = MC/I was used. Four main wing structures were considered to add bending strength: Circular Spar, Rectangular Spar, C-Channel, and Parallel Split Spar, as shown in Figure 9.1.1.



Figure 9.1.1: Proposed Spar Configurations

For weight comparison purposes, each shape was analyzed as if it had a 1 in² cross section, and the maximum bending stress was calculated using $\sigma = MC/I$. The moment used was derived from the fluid analysis. The distributed load on the wing during flight is calculated to be 0.01134 psi. To be conservative, the wing load is applied as a point load at the ends of the wing. This results in a 15.65 lb force at 6 ft, giving a moment of 1127 in-lbs. The results are tabulated below in Table 9.1.1.

Table 9.1.1: Spar Shape Comparison

Shape	Inertia (in ⁴)	Maximum Experienced Bending Stress (psi)
Square cross Section	.083	6763
Circular Cross Section	.080	2995
Channel	1.036	1631
Parallel Spars	1.864	580

The parallel spars experienced the lowest bending stress, so this design was chosen. Thus, the spars used were sized $\frac{3}{8}$ in by $\frac{5}{8}$ in, giving a final factor of safety of 4.51. This gives a maximum deflection of 2.27". Additional stringers are added for stiffness, torsion resistance, and monokote attachment.

9.2 Tail

For the tail section, similar logic was utilized to select the support structure design. The distributed load on the tail is 0.00831 psi. To be conservative, the moment is assumed to be the entire distributed load applied at the ends of the tail. This results in a 1.65 lbf at 3ft (36 in), giving a moment of 59.4 in-lbs. The parallel spar design is also used in the tail section, with sizes $\frac{1}{2}$ " by $\frac{1}{4}$ ". Like the wing, additional stringers are added for extra support. To minimize deflection, the spars are oversized, giving a deflection of .01" with a FS of 5.22.

9.3 Tube

Various boom designs were considered for this plane. Wood and aluminum were considered. However, tests revealed that wood experienced large deflections when flight loads were applied. Then, aluminum was considered. For torsional stiffness and strength, a circular tube is the optimum shape.

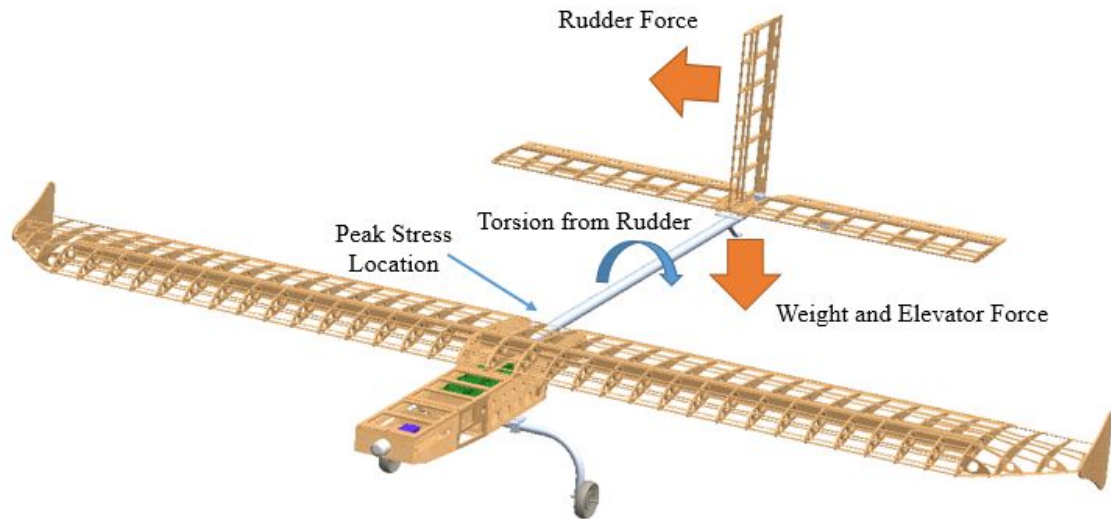


Figure 9.3.1: Tube Load Application

There is significant dynamic load between the wing and the tail. Torsion from rudder movement, bending from aircraft weight, bending from rudder movement, and bending from elevator movement all apply. Fluid analysis provides loads shown below. Each load is modeled as a worst case scenario with loads described in Section 8.

Table 9.3.1 Tube Stresses

Type	Cause	Moment (in lbs)	Stress Induced (psi)
Bending	Elevator	140.4	2918
Bending	Weight	108.0	2245
Bending	Rudder	58.5	1216
Torsion	Rudder	12.6	131

VM Equivalent Stress	3880	psi
Yield Strength of 6061 Aluminum	40000	psi
Factor of Safety	10.3	

Deflection was also calculated, and the size was altered to reduce the deflection to 1.08 in and 1.4 degrees. A smaller size could have been chosen to reduce FS and weight without yielding. However, this would have had a large deflection which would hurt plane performance.

9.4 Landing Gear

The landing gear was analyzed using a load derived from the impact created by a hard landing, 100 lbs. To be conservative, this load was applied to one side of the landing gear, assuming uneven

landing. To size the landing gear tube, both shear and bending stresses were considered. The Von Mises equivalent stress was considered for the factor of safety. The landing gear was modeled as a cantilever beam with a 50 lb load applied at the wheel distance, 12 inches from center. The final size is 1” outer diameter with a .095” wall thickness.

Table 9.4.1 Landing Gear Stresses

Shear Stress on Cross Section	185.2	psi
Bending Stress at Center	21473	psi
Von Mises Equivalent	21473	psi
6061-T6 Aluminum Yield Strength	30000	psi
Factor of Safety	1.40	

10.0 Servo Sizing

Servos were sized based on the control surface loads calculated in Section 8 and the linkage geometry connecting the servos to the control surfaces. All control surfaces are actuated by a rigid control rod connected directly to a servo. The highest torque that a servo must deliver to a control surface occurs at that surface’s maximum deflection, 40 degrees. Tracing a control surface load through the control linkage yields the torque a given servo needs to deliver. 188 oz-in servos were found to be suitable for all control surfaces. One servo is used to control each control surface, except the elevator. Since the elevator is split in half to allow for rudder movement, one servo is used to control each side of the elevator and only needs to deliver half the torque necessary for the entire surface. Table 10.0.1 details the torque each servo needs to deliver and the factor of safety for each.

Table 10.0.1: Necessary Servo Torques for Control Surfaces

Control Surface	Necessary Torque (in-lbs)	Factor of Safety
Elevator (one half)	7.05	1.67
Rudder	5.88	2.00
Aileron	10.38	1.14

11.0 Conclusions

The final design was completed within the parameters set by the SAE Aero Design Challenge. year's plane is a mono-wing plane with a 12 foot wingspan and backward sweep. The projected flight score per round is 68.7 carrying 22 balls and 11 pounds of luggage, which was verified by testing.

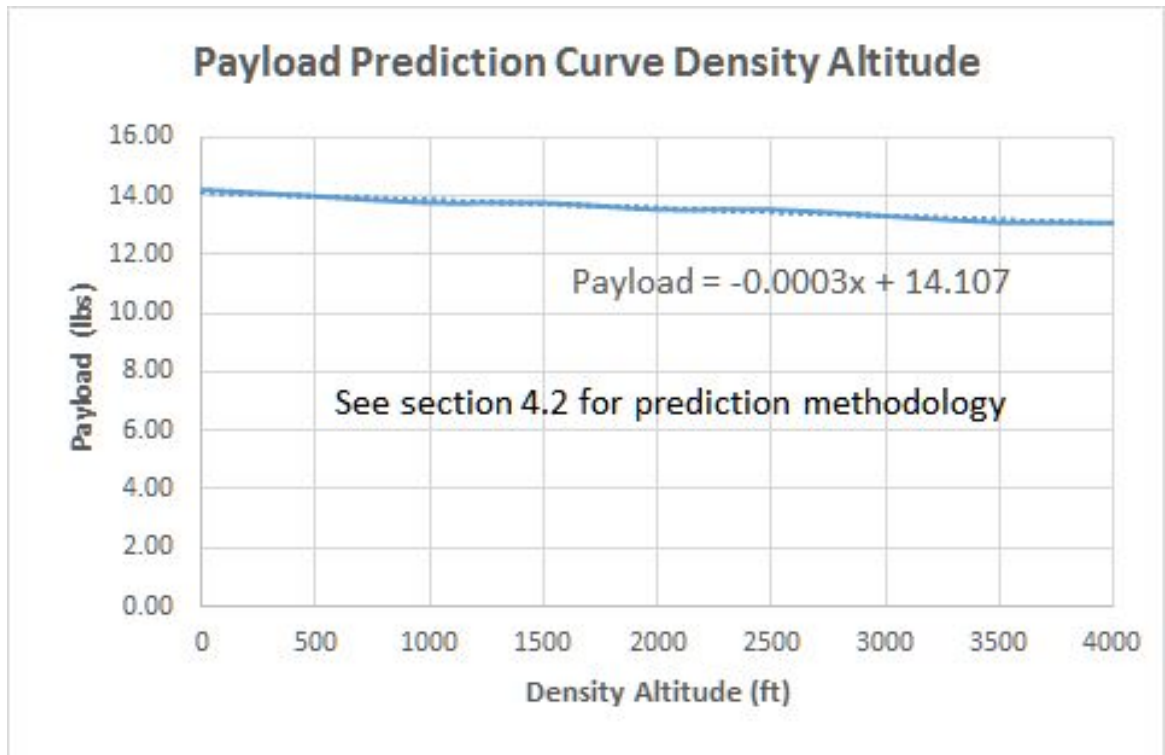
12.0 Table of Referenced Documents, References, and Specifications

#	Source	Use
1	http://m-selig.ae.illinois.edu/ads/coord_database.html	Airfoil Data Points
2	Cengel and Cimbala, Essentials of Fluid Mechanics: Fundamentals and Applications	Lift and Drag Calculations
3	https://www.grc.nasa.gov/www/k-12/airplane/lifteq.html	Lift and Drag Calculations
4	Aircraft Structures: David J Peery	Structural Design and Analysis
5	Airframe Stress Analysis and Sizing: Niu	Structural Design and Analysis
6	https://www.faa.gov/uas/getting_started/	Federal Aviation Administration Standards
7	Propeller Static & Dynamic Thrust Calculation: Gabriel Staples	Thrust Analysis
8	Aircraft Landing Gear Layouts: Scott, Jeffrey A.	Landing gear placement

List of Symbols and Acronyms

2D	Two dimensional	V(v)	Velocity
3D	Three dimensional	v	Initial velocity
A	Area	V	Max Velocity
a	Acceleration	W	Weight
C_D	Drag coefficient	X	Final distance
CFD	Computational Fluid Dynamics	x	Initial distance
C_L	Lift coefficient	μ	Dynamic viscosity
D(v)	Drag	TU	University of Tulsa
f(v)	Friction between the airplane and runway	kV	rpm/Volt
L	Lift	rpm	Revolutions per Minute
NACA	National Advisory Committee for Aeronautics	mAh	milliamp hours
T(v)	Dynamic Thrust Generated by Propeller	ESC	Electronic Speed Controller
$T_{net}(v)$	Net Thrust	ρ	Density
t	Time	p_0	Air pressure at sea level

Appendix A: Payload Prediction Curve Density Altitude



Appendix B: 2D Drawing

